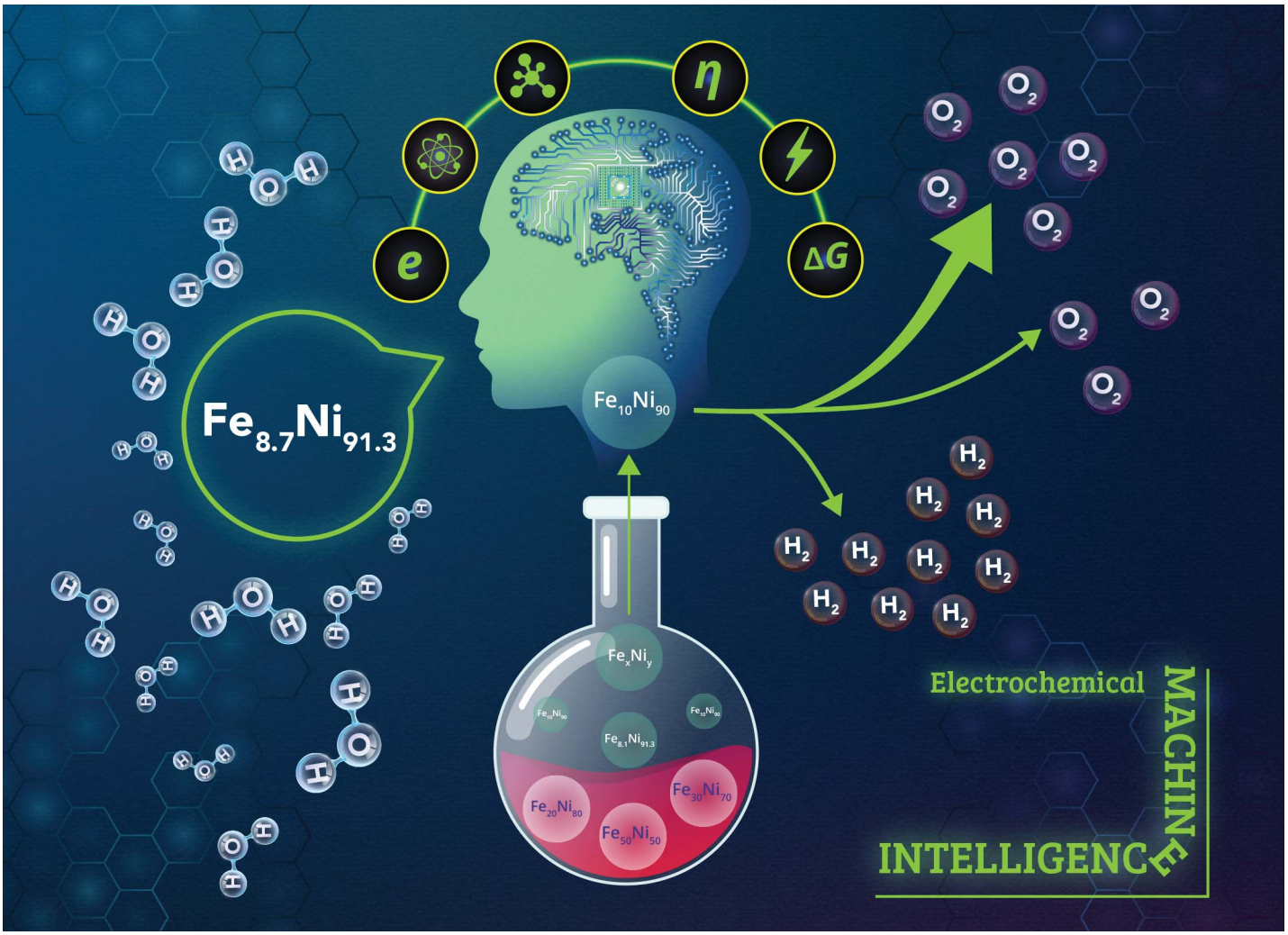

Machine learning with its experimental observations takes place at the Ertl Center for Electrochemistry and Catalysis and the Electrochemical Reaction and Technology Laboratory (ERTL) in Gwangju, South Korea.

Non-noble electrocatalysts discovered by scaling relations of Gibbs-free energies of key oxygen adsorbates in water oxidation

Electrochemical artificial machine intelligence reveals the very exact ratio of iron element in FeNi composite catalysts. It could improve electrolytic energy efficiency in the challenging process of alkaline water oxidation.

As featured in:

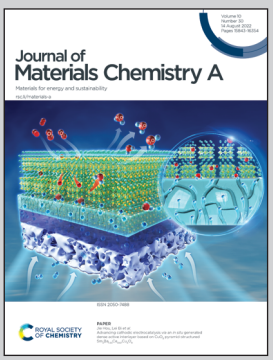

See Jaeyoung Lee *et al.*, *J. Mater. Chem. A*, 2022, **10**, 15975.

ROYAL SOCIETY OF CHEMISTRY

rsc.li/materials-a

Registered charity number: 207890

Journal of Materials Chemistry A

ROYAL SOCIETY OF CHEMISTRY

PAPER

View Article Online
View Journal | View Issue

Cite this: J. Mater. Chem. A, 2022, 10, 15975

Non-noble electrocatalysts discovered by scaling relations of Gibbs-free energies of key oxygen adsorbates in water oxidation†

Jihyeon Park,[ab] Sinwoo Kang[ab] and Jaeyoung Lee *[abc]

Received 31st March 2022
Accepted 29th June 2022

DOI: 10.1039/d2ta02594a

rsc.li/materials-a

Symbolic regression (SR) is the most widely used machine learning (ML) tool for determining the governing equation from a given dataset. However, a major problem associated with SR is gaps in the results (missing results) when more mathematical operations are introduced. We applied deep symbolic regression (DSR) to a dense space of overpotential formulas to reveal the scaling relations of the Gibbs free energies of the key intermediate adsorbates during the oxygen evolution reaction (OER) on FeNi surfaces in alkaline media. The highest-ranked empirical equation $f(x)$ generated from 40 000 000 hidden equations by DSR predicted an optimized electrocatalyst ratio of $Fe_{8.7}$: $Ni_{91.3}$, which resulted in a minimum overpotential of 0.368 V in the water-splitting process. Our approach provides a new perspective for understanding nonlinear dynamics in the electrochemical processes of chemical-energy conversion and storage.

1 Introduction

Electrocatalytic water splitting in alkaline media is one of the most eco-friendly methods for producing hydrogen; however, the biggest obstacle to its commercialization is the sluggish oxygen evolution reaction (OER).[1–4] This is because the OER is a four-electron process that proceeds through various adsorption processes and intermediate species, including *OH, *O, and *OOH.[5,6] Although the binding energy between the adsorbates and catalyst surfaces shows a variety of remarkable linear correlations,[7–11] it is difficult to optimize them independently because the entire process is systematically related. The scaling relationships between the adsorption energies and various descriptors suggest a research direction for developing a well-performing catalyst for the OER. In particular, the scaling relations between the Gibbs free energies of the key adsorbates (*OH and *OOH) suggest a research direction for developing a well-performing catalyst for the OER. However, even in FeNi-based catalysts, which rank as the best-performing non-precious-metal catalysts, the minimum overpotential is limited to approximately 0.37 V.[5,12–18] Therefore, many researchers have reported that they broke the scaling relations by designing highly active OER catalysts.

The conventional trial-and-error method for synthesizing catalysts with high activities has the advantage of providing experimental data for the developed materials and catalytic performances. Thus, meaningful perspectives can be gained from practical results. However, the trial-and-error method is a time-consuming process, expensive, and difficult to control precisely.[19–21] In contrast, computational strategies such as density functional theory (DFT) are very useful for the rapid screening of an enormous number of catalyst candidates. However, since most DFT calculations are based on an ideal combination of absorbates and crystal structures, the actual experimental results are difficult to correlate with the various descriptors.[22,23] Therefore, if the actual OER results and various descriptors could be associated from a computational standpoint, a more effective method can be derived.

However, it is challenging to consider both the interdependence of each step in the OER and the various descriptors simultaneously. In particular, when using symbolic regression (SR), which aims to elucidate the relationships between variables,[24–26] the number of possible functions increases exponentially as the number of variables and the types of mathematical operations used in the SR increase. Such a process is time-consuming and can inadvertently cause the occurrence of gaps (missing results) in the list of generated formulas.

Deep symbolic regression (DSR) is an algorithm that combines deep learning (DL) with SR to overcome the shortcomings of SR.[27] DL, which has the characteristic of improved performance as learning progresses, penetrates deep into the gaps between the formulas created by SR. Therefore, in DSR, the performance in

[a]School of Earth Sciences and Environmental Engineering, Gwangju Institute of Science and Technology, 123 Cheomdangwagi-ro, Buk-gu, Gwangju 61005, South Korea. E-mail: jaeyoung@gist.ac.kr

[b]International Future Research Center of Chemical Energy Storage and Conversion Processes, Gwangju Institute of Science and Technology, 123 Cheomdangwagi-ro, Buk-gu, Gwangju 61005, South Korea

[c]Ertl Center for Electrochemistry and Catalysis, Gwangju Institute of Science and Technology, 123 Cheomdangwagi-ro, Buk-gu, Gwangju 61005, South Korea

† Electronic supplementary information (ESI) available. See https://doi.org/10.1039/d2ta02594a

expressing the target value gradually improves as the algorithm proceeds with the increased spatial density of the equations.

In this study, we first employed the DSR algorithm to find correlations between actual experimental results and physical/calculative properties through the DSR algorithm. $FeNiO_xH_y$ has the highest activity among non-precious-metal catalysts, and seven samples of this catalyst were synthesized with different contents of Fe and Ni using electrodeposition. The catalytic activity data for $FeNiO_xH_y$ (needed for the DSR algorithm) was obtained from our cyclic voltammetry (CV) tests on the seven catalysts, while the physical/calculative property data was obtained from other references.

2 Materials and methods

2.1 Synthesis of $FeNiO_xH_y$

The catalyst films were synthesized *via* electrodeposition according to a previously reported method.[28–30] Nickel nitrate ($Ni(NO_3)_2$, Sigma-Aldrich) and iron chloride ($FeCl_2 \cdot H_2O$) were dissolved in deionized water to prepare the electrodeposition solution. The total concentration of the metal precursor solution used was 0.1 M. In this study, the ratio of Ni to Fe followed the precursor ratio, which was confirmed by energy-dispersive X-ray electron microscopy (*e.g.*, $Fe_{10}Ni_{90}O_xH_y$ means that the catalyst film was prepared using a solution of 10% nickel nitrate and 90% iron nitrate). Ni_{100}, $Fe_{10}Ni_{90}$, $Fe_{20}Ni_{80}$, $Fe_{30}Ni_{70}$, $Fe_{50}Ni_{50}$, $Fe_{70}Ni_{30}$, and Fe_{100} constituted a standard set prepared for the database. After bubbling the solution with N_2 for 30 min to prevent FeO_x precipitation, electrodeposition was conducted in a two-electrode system. The gas diffusion layer (GDL; MGL 190, AvCarb), used as the working electrode, was cut to dimensions of 1 cm × 1 cm (excluding the connecting part with the gold screw electrode). Carbon cloth was used as a counter-electrode to provide a sufficient working area, while preventing the dissolution of Pt wire. The deposition and electrochemical reaction areas were calculated to be 2 cm^2, in consideration of both the front and back sides of the GDL. Electrodeposition was conducted at an applied current of −2.5 mA cm^{-2} for 30 s. Fe_5Ni_{95}, $Fe_{15}Ni_{85}$, and $Fe_{25}Ni_{75}$ were also prepared for validating the empirical equation.

2.2 Electrochemical characterization

A potentio/galvanostat (VSP, Bio-Logic) was used for electrochemical characterization in a polyether ether ketone (PEEK) cell. PEEK prevents both oxygen adsorption and penetration through the walls, thus minimizing oxygen-related issues.[31] All measurements were performed in 0.1 M Fe-free KOH, as adopted from the purification method reported by Boettcher *et al.*[30] A graphite rod was used as a counter-electrode instead of the widely used Pt mesh because of the Pt dissolution issue[32,33] and a Hg/HgO electrode with 1 M KOH filling solution was used as the reference electrode. Cyclic voltammetry (CV) curves were acquired at a scan rate of 5 mV s^{-1}, and the *iR* drop was compensated by 85% using Bio-Logic EC-Lab software. The working electrode applied a potential from 0 to 1 $V_{vs.\ Hg/HgO}$ with both anodic and cathodic sweeps per cycle. Tafel plots were acquired free of *iR* drop at a low scan rate (5 mV s^{-1}) to suppress capacitive current.[34] Electrochemical impedance spectroscopy was performed at 1.7 $V_{vs.\ RHE}$ by applying a voltage with an amplitude of 10 mV in the frequency range from 100 kHz to 100 MHz. All measurements in this study are presented in terms of the reversible hydrogen electrode (RHE) scale using the equation: $E(V_{vs.\ RHE}) = E(V_{vs.\ Hg/HgO}) + 0.098 + 0.095 \times pH$.

2.3 Preparation of properties for database

Properties involving Ni : Fe ratios were calculated from linear relationships based on those of pure Ni and pure Fe. For example, a property (X_i) of $Fe_aNi_{(1-a)}O_xH_y$ was calculated from $aX_i^{Fe} + (1-a)X_i^{Ni}$. In addition, the active oxidation state for the OER was carefully considered when Ni and Fe were combined.[35–38] The number of d-electrons (N_d), atomic radii (γ), and Pauling electronegativity (χ) are listed in Table S2† as functions of the oxidation state. In alkaline water electrolysis, the adsorption energy for each reaction step remains the subject of controversy;[15,17,39,40] however, the most widely accepted four-step reaction was used (eqn (1)–(4)).[41,42]

$$\Delta G_1 = \Delta G_{OH} \quad (1)$$

$$\Delta G_2 = \Delta G_O - \Delta G_{OH} \quad (2)$$

$$\Delta G_3 = \Delta G_{OOH} - \Delta G_O \quad (3)$$

$$\Delta G_4 = \Delta G_{O_2} - \Delta G_{OOH} \quad (4)$$

Eqn (5) and (6) were used to calculate $\max(\Delta G_i)$ and the electrochemical step symmetric index (ESSI), respectively, as follows.[43]

$$\max(\Delta G_i) = \frac{\max \Delta G_i}{e^-} - 1.23 \quad (5)$$

$$\mathrm{ESSI} = \frac{1}{n}\sum_1^n \left(\frac{\Delta G_i{}^+}{e^-} - 1.23\right), \text{ where } \Delta G_i{}^+ := \Delta G_i > 1.23 \quad (6)$$

2.4 Physical characterization

The surface morphology of the electrodeposited samples was examined using field-emission scanning electron microscopy (FE-SEM; Hitachi, S-4700). The surface binding energy of the sampled metal oxide on the carbon paper was analyzed by high-performance X-ray photoelectron spectroscopy using an Al Kα X-ray source (HP-XPS; Thermo-Fisher). All the binding energies were fitted based on the C 1s reference (285.0 eV) using Avantage software. Grazing incidence X-ray diffraction (GI-XRD) analysis (DMAX2500-PC, Rigaku) was used to evaluate the crystallinity of the ultrathin surfaces of the samples.

3 Results and discussion

The prepared database was divided into four parts according to the current density (1, 5, 10, and 20 mA cm^{-2}) and input into the DSR algorithm. All databases included nine properties (X_i: N_d,

γ, χ, ΔG_1 to ΔG_4, max(ΔG_i), and ESSI) and one object value, overpotential ($y_i : \eta$). All mathematical equations from the DSR algorithm were aimed at determining the best function to represent the object value (eqn (7)).

$$\text{dataset } (X_i \in R^n,\ y_i \in R),\ \text{function } f{:}R^n \rightarrow R \tag{7}$$

The equations generated by the DSR algorithm can be expressed as hierarchical symbolic trees. The tree branch designated "node", as shown in Fig. S2,† has three types. Mathematical operations, including +, −, ×, and ÷, which require two variables, are represented by light-yellow nodes. In contrast, mathematical operations, including exp, ln, $\sqrt{x}$, x^2, sin, and cos, which require one variable, are represented by sky-blue nodes. The terminals whose branches no longer extend are represented by gray nodes.

The input database goes through a recurrent neural network (RNN), and the DSR algorithm performs mathematical operations step-by-step until the equation is completed. Notably, the mathematical operations sampled at each step are not randomly emitted by independent trials but depend on the probability (p) of the mathematical operations at all previous steps. In other words, the probability is directly proportional to the success of each attempt as evaluated in the previous steps. That is, the i^{th} mathematical expression (τ_i) can be expressed by the probability vector (ψ), including all previous expressions ($\tau_{1:i-1}$) and the RNN internal parameters (θ) (eqn (8)), and the probability of the function at that time is identical to the product of the probabilities of all steps (eqn (9)). Further details can be found in ref. 27.

$$p(\tau_i|\tau_{1:i-1},\ \theta) = \psi^{(i)}_{\mathscr{D}(\tau_i)} \tag{8}$$

$$p(\tau|\theta) = \prod_{i=1}^{|\tau|} \psi^{(i)}_{\mathcal{L}(\tau_i)} \tag{9}$$

However, because the functions have a hierarchical-tree structure, there are several restrictions in the equation expression stage of the DSR algorithm. First, the expression length of the mathematical equation must not be less than 4 or more than 30 parameters. If the length was less than 4, the equation would likely be too simple to be accurate, and if the length was more than 30, the equation would become too complex to interpret intuitively. The second restriction is that the children of the operator cannot all be constraints ($\mathbb{C}$). If this was allowed, the results would still be constrained (*e.g.*, $\sin(\mathbb{C}) = \mathbb{C}$, $\mathbb{C} \times \mathbb{C} = \mathbb{C}$). The third restriction is related to the operator, which requires one variable and states that a child operator should not be an inverse function of its parent (*e.g.*, $\sqrt{x^2}$, $e^{\ln(x)}$). The last restriction is that a trigonometric operator should not have a descendant because such expressions cannot be found in nature (*e.g.*, $\sin(x + \cos(x))$).

Fig. 1a shows a structural diagram of the DSR algorithm, which generates an equation for expressing the overpotential at a specific current density of 10 mA cm^{-2}. The preprocessed database with the physical and calculative properties is applied to the DSR algorithm, and the algorithm constantly attempts to create an equation expressing the overpotential with these properties. In this situation, the equation is created in a hierarchical process inside the DSR algorithm, which can be expressed as a tree structure (Fig. S2†). However, this is only a schematic explaining the structure of the algorithm, and in practice, a complete equation is produced by the algorithm, as shown in eqn (10). Therefore, it is difficult to determine how a completed equation is calculated and produced by the DSR algorithm, which is also a representative feature of deep learning.

$$\eta^{\text{empirical}}_{10\text{ mA cm}^{-2}}(X_i) = e^{\sin\left(\ln\left(\ln\left(\sqrt{\max(\Delta G_i)} + \frac{\text{ESSI}}{\max(\Delta G_i)}\right)\right)\right)} \tag{10}$$

The DSR algorithm produces 4000 different equations at each step and evaluates them simultaneously. The normalized root-mean-square error (NRMSE) of the overpotential is calculated using the empirical overpotential ($\hat{y}$) and actual overpotential (y) at a specific current density of 10 mA cm^{-2} was calculated and rated using eqn (S1) and (S2),† respectively. The closer the precision score is to 1, the higher the accuracy. The blue open circles in Fig. 1b represent the maximum score among the 4000 equations for each step, and the red solid line represents the best score in all the previous steps. As the number of learning steps increases, the maximum and best scores also increase, indicating that the RNN inside the DSR algorithm conducts reinforcement learning of the previous step and gradually improves the performance to generate empirical equations with increasing number of steps. It seems that if more time is consumed, better empirical equations with higher

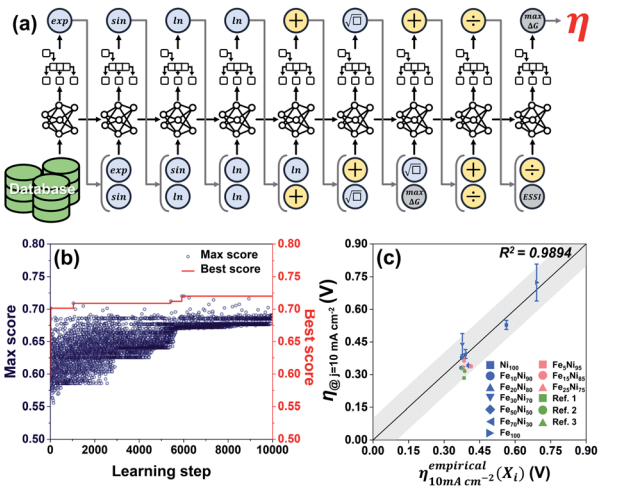

Fig. 1 (a) Hierarchical internal algorithm structure of the deep symbolic regression (DSR) that generates the completed equation with three different node types: yellow (binary), sky-blue (unary), and gray (terminal). Database is DSR input and the empirical equation is DSR output; (b) precision score graph as a function of the number of learning steps (max score is the maximum precision score of 4000 different equations per step, and best score is the best precision score in all previous steps); and (c) reformatted graph based on the final best equation with a gray solid line corresponding to the $y = x \pm 0.1$ graph (Ref. 1: 44, Ref. 2: 45,and Ref. 3: 46).

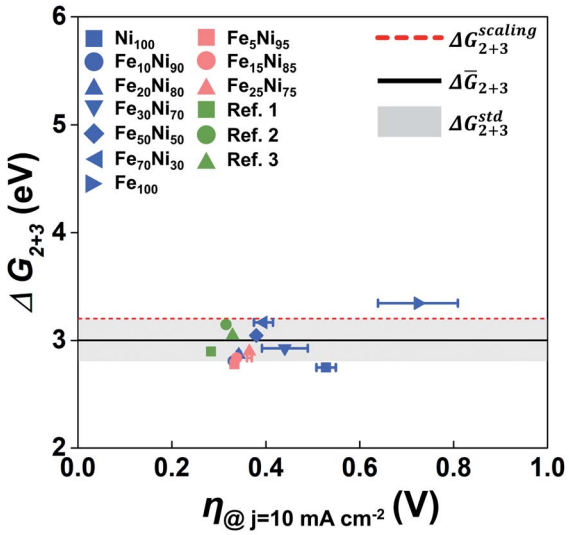

Fig. 2 The sum of adsorption steps 2 and 3 (ΔG_{2+3}) as a function of the overpotential (at 10 mA cm^{-2}), the dashed red line corresponds to the conventional scaling relationship value of 3.2 eV ($\Delta G_{2+3}^{scaling}$), the solid black line and the gray zone correspond to the mean value of ΔG_{2+3} of all prepared catalyst ($\Delta \bar{G}_{2+3} = 3.001$ eV) and the standard deviation of ΔG_{2+3} of all prepared catalyst ($\Delta G_{2+3}^{std} = 0.195$ eV), respectively.

precision scores are created. Furthermore, when a parameter was excluded from eqn (10) to confirm the parameter effect, the NRMSE score increased, and the empirical equation became extremely complicated, with a low R^2 value (Table S5†).

The top 50 equations with their scores are shown in the ESI.† The top-ranked empirical equation expressing the overpotential is the same as that shown in eqn (10), with an NRMSE score of 0.7201. To precisely show the correlation, the overpotential calculated using eqn (10) and the actual overpotential at 10 mA cm^{-2} are shown in Fig. 1c, with an added gray graph of $y = x \pm 0.1$. The average and standard error values of the overpotentials for each Fe : Ni ratio in $FeNiO_xH_y$ in the database are represented by blue symbols and error bars, respectively. All the blue symbols are close to the $y = x$ graph, indicating that the empirical equation was successful in describing the data. Furthermore, the top-ranked empirical equation also fits the results from additional experiments (pink symbols), as well as from other reference data (pea-green symbols), showing a high R^2 of 0.9894. Moreover, the empirical equations obtained *via* the DSR algorithm were also reformatted and plotted at current densities of 1, 5, and 20 mA cm^{-2}, which were then verified by additional experiments (Fig. S3†).

Since a deep learning-based algorithm was used, the top-ranked empirical equation expressing the overpotential at 10 mA cm^{-2}, which is a representative method for OER performance, is difficult to understand intuitively. The equation includes only two calculative properties (max(ΔG_i) and ESSI); therefore, it was unclear in which direction we should drive our research to further lower the overpotential. To evaluate this instinctively, the equation was expressed as a three-dimensional (3D) graph (Fig. S4†). Although the overpotential value oscillates owing to the trigonometric function, the graph indicates that we

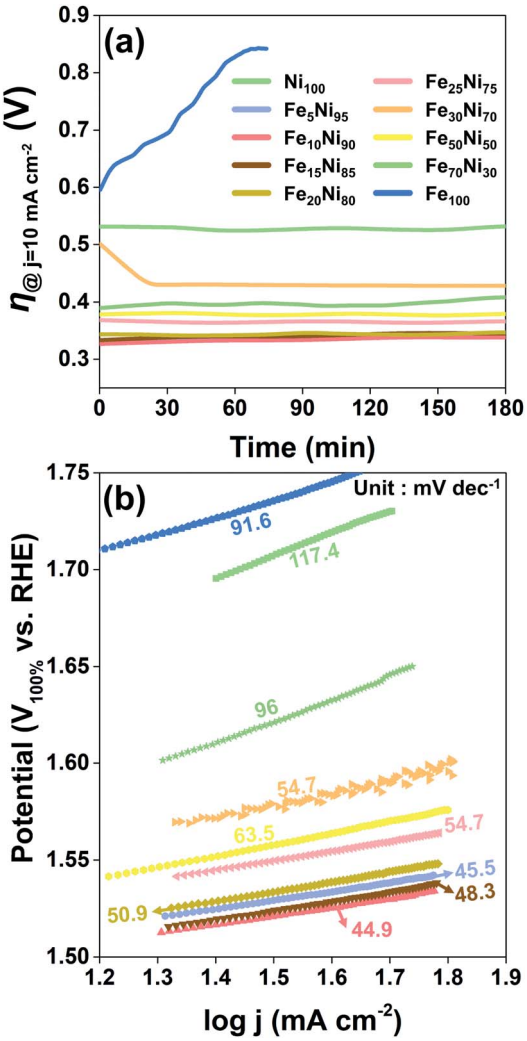

Fig. 3 (a) Chronoamperometry tests conducted at 10 mA cm^{-2} *vs.* RHE at the controlled temperature of 25 °C in 1 M KOH for 180 min; and (b) Tafel plots and slopes of $FeNiO_xH_y$ acquired free of *iR* drop at a low scan rate of 5 mV s^{-1} to suppress capacitive current.

should seek to reduce both max(ΔG_i) and ESSI. However, the minimum value of the overpotential is limited to $e^{-1} = 0.368$ V due to the synthesis function of exp and sin.

For an ideal OER catalyst, all adsorption energies (ΔG_i) should be identical (1.23 eV), and the sum of ΔG_2 and ΔG_3 should be 2.46 eV ($\Delta G_{2+3} = \Delta G_{OOH} - \Delta G_{OH}$). However, in the real world, the average value of ΔG_{2+3} in a large group of OER catalysts is usually 3.2 ± 0.2 eV, irrespective of the overpotential, as shown in Fig. 2.[43–48] Interestingly, even if most of the OER overpotentials are affected by ΔG_2 or ΔG_3, the minimum value of the empirical equation to break the scaling relationship could still not break the "great wall of the scaling relationship". It is impressive to observe the natural limiting overpotential in the actual OER environment determined *via* artificial intelligence (eqn (11)). Furthermore, this suggests that there is no correlation between breaking the scaling relation and lowering the overpotential.[10,43]

$$e^{-1} = 0.368\ \text{V} \approx (3.2\text{–}2.46)\ \text{eV}/2\text{e}^- \quad (11)$$

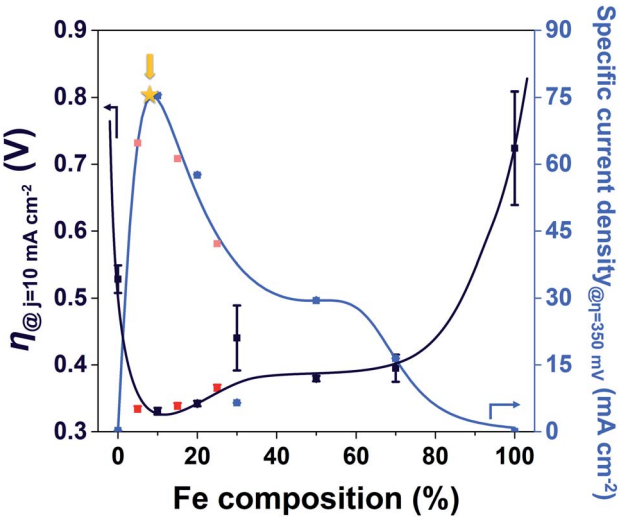

Fig. 4 OER performance and overpotential of $FeNiO_xH_y$ catalysts achieved at η of 350 mV and j of 10 mA cm^{-2}, respectively, as a function of Fe composition; blue and indigo-blue (Ni_{100}, $Fe_{10}Ni_{90}$, $Fe_{20}Ni_{80}$, $Fe_{30}Ni_{70}$, $Fe_{50}Ni_{50}$, $Fe_{70}Ni_{30}$, and Fe_{100} for database), pink and red (Fe_5Ni_{95}, $Fe_{15}Ni_{85}$, and $Fe_{25}Ni_{75}$ for validation). The gold star represents DSR-derived ratio of $Fe_{8.7}Ni_{91.3}$.

In the forward scan, an oxidation peak of Ni was present until the Fe content reached 25% (Fig. S5†). We only collected results for the database in the backward scan to avoid any interference from this oxidation peak. The current density at the same potential increases until the Fe content reaches 10% and decreases as the Fe content exceeds 10%. The best $Fe_{10}Ni_{90}$ electrode retained its low overpotential with an increase of only 2.51 μV per minute (*i.e.*, a 0.00273% overpotential increase per minute) (Fig. 3a).

The slope range of the Tafel plot in the Fe range 5–20% is 45–50 mV dec^{-1}, exhibiting a clear difference from that in the other ratios (Fig. 3b). Therefore, to reduce the overpotential in a practical water electrolysis cell/stack, it is not necessary to use a catalyst with a specific ratio such as the ideal 8.7% as determined from Fig. 4. Instead, any $FeNiO_xH_y$ catalyst with an Fe content between 5% and 20% with respect to Ni should be sufficient.

From the CV cycles of the mixed ratios of $FeNiO_xH_y$ (Fig. S5†), two features were extracted as a function of Fe content: one for the previously mentioned overpotential at a current density of 10 mA cm^{-2}, and the other for the specific current density at an overpotential of 350 mV (Fig. 4). Thus, as the Fe content is increased in the range 5–20%, the overpotential decreases and then increases, and the specific current density increases and then decreases, covering the local minimum and maximum of overpotential and current density, respectively. This result is comparable to recent works in which Fe_xNi_{1-x} ($0 < x < 0.25$) is mainly considered to be at the maximized activity.[18,49]

The measured overpotential ranges from 0.3 to 0.35 V, which is lower than those in the other ranges, and the measured specific current density is 4–9 times higher than those in the other ranges (also see Fig. S6†). To determine the ideal ratio, we used the DSR algorithm again, but in terms of specific current density. Notably, the variables and target values for the algorithm were the Fe content and specific current density (at 350 mV), respectively. The detailed conditions and equations are listed in Table S1 and eqn (S3),† respectively. From the differential value of the empirical equation, the ideal Fe content was calculated to be 8.7% (gold star in Fig. 4 and eqn (S4)†), which is close to that obtained by density functional theory (DFT) calculations, as reported by the Goddard III group.[38] They confirmed that the overpotential for the OER was higher when the bulk Fe content in FeNi was approximately 1/9.

4 Conclusions

In summary, we used a DSR algorithm to find the hidden empirical equations of the OER based on the physical (N_d,γ,χ) and calculative properties (ΔG_1 to ΔG_4, max(ΔG_i), ESSI) of $FeNiO_xH_y$. A top-ranked equation expressing the overpotential at 10 mA cm^{-2} among 40 000 000 formulas was generated using Gibbs free energies (max(ΔG_i)) and ESSI. To confirm whether the created equation was well fitted, we synthesized several intermediate ratios (Fe_5Ni_{95}, $Fe_{15}Ni_{85}$, and $Fe_{25}Ni_{75}$) and obtained the overpotentials from other references, confirming a high R^2 of 0.9894. We concluded that the equation successfully predicted the overpotentials for our additional experiments, as well as for the unlearned data. FeNi catalysts with an Fe content of 5–20% exhibited long-term stability and a low Tafel plot slope. Surprisingly, the minimum value of the overpotential function generated by DSR was e^{-1} (= 0.37 V), which is nearly identical to that obtained from the scaling relation. Finally, the algorithm derived the optimal ratio of Fe : Ni as 8.7 : 91.3. Our approach provides a new perspective for interpreting electrochemistry using artificial intelligence and may lead to improvements in catalyst design for water electrolysis.

Author contributions

J. P. designed the computational framework and performed the machine learning calculations. S. K. supported additional experimental observations. J. P. and J. L. was in charge of overall direction and planning.

Conflicts of interest

There are no conflicts to declare.

Acknowledgements

This research was supported by the National R&D Program through the National Research Foundation of Korea (NRF) funded by the Ministry of Science and ICT (NRF-2021K1A4A8A01079455) and this work was supported by AI-based GIST Research Scientist Project grant funded by GIST in 2022.

Notes and references

1 J. A. Turner, *Science*, 2004, **305**, 972–974.

2 I. Katsounaros, S. Cherevko, A. R. Zeradjanin and K. J. J. Mayrhofer, *Angew. Chem., Int. Ed.*, 2014, **53**, 102–121.
3 S. Kang, K. Ham and J. Lee, *Electrochim. Acta*, 2020, **353**, 136521.
4 K. Ham, S. Hong, S. Kang, K. Cho and J. Lee, *ACS Energy Lett.*, 2021, **6**, 364–370.
5 Z.-F. Huang, J. Song, S. Dou, X. Li, J. Wang and X. Wang, *Matter*, 2019, **1**, 1494–1518.
6 D. Zhou, S. Wang, Y. Jia, X. Xiong, H. Yang, S. Liu, J. Tang, J. Zhang, D. Liu, L. Zheng, Y. Kuang, X. Sun and B. Liu, *Angew. Chem., Int. Ed.*, 2019, **58**, 736–740.
7 M. M. Montemore and J. Will Medlin, *Catal. Sci. Technol.*, 2014, **4**, 3748–3761.
8 F. Abild-Pedersen, J. Greeley, F. Studt, J. Rossmeisl, T. R. Munter, P. G. Moses, E. Skúlason, T. Bligaard and J. K. Nørskov, *Phys. Rev. Lett.*, 2007, **99**, 016105.
9 F. Calle-Vallejo, D. Loffreda, M. T. M. Koper and P. Sautet, *Nat. Chem.*, 2015, **7**, 403–410.
10 K. S. Exner, *Chem*, 2021, **1**, 258–271.
11 B. Garlyyev, J. Fichtner, O. Piqué, O. Schneider, A. S. Bandarenka and F. Calle-Vallejo, *Chem. Sci.*, 2019, **10**, 8060–8075.
12 M. T. M. Koper, *Chem. Sci.*, 2013, **4**, 2710–2723.
13 C. Roy, B. Sebok, S. B. Scott, E. M. Fiordaliso, J. E. Sørensen, A. Bodin, D. B. Trimarco, C. D. Damsgaard, P. C. K. Vesborg, O. Hansen, I. E. L. Stephens, J. Kibsgaard and I. Chorkendorff, *Nat. Catal.*, 2018, **1**, 820–829.
14 W. Zhang, D. Li, L. Zhang, X. She and D. Yang, *J. Energy Chem.*, 2019, **39**, 39–53.
15 Y.-F. Li and A. Selloni, *ACS Catal.*, 2014, **4**, 1148–1153.
16 Y. Zhou and N. López, *ACS Catal.*, 2020, **10**, 6254–6261.
17 J. Wang, Y. Gao, H. Kong, J. Kim, S. Choi, F. Ciucci, Y. Hao, S. Yang, Z. Shao and J. Lim, *Chem. Soc. Rev.*, 2020, **49**, 9154–9196.
18 D. Friebel, M. W. Louie, M. Bajdich, K. E. Sanwald, Y. Cai, A. M. Wise, M.-J. Cheng, D. Sokaras, T.-C. Weng, R. Alonso-Mori, R. C. Davis, J. R. Bargar, J. K. Nørskov, A. Nilsson and A. T. Bell, *J. Am. Chem. Soc.*, 2015, **137**, 1305–1313.
19 H. J. Kim, H. Y. Kim, J. Joo, S. H. Joo, J. S. Lim, J. Lee, H. Huang, M. Shao, J. Hu, J. Y. Kim, B. J. Min, S. W. Lee, M. Kang, K. Lee, S. Choi, Y. Park, Y. Wang, J. Li, Z. Zhang, J. Ma and S.-I. Choi, *J. Mater. Chem. A*, 2022, **10**, 50–88.
20 L. X. Chen, Z. W. Chen, M. Jiang, Z. Lu, C. Gao, G. Cai and C. V. Singh, *J. Mater. Chem. A*, 2021, **9**, 2018–2042.
21 Z. Zhou, *J. Mater. Chem. A*, 2021, **9**, 1295–1296.
22 D. Y. Kim, M. Ha and K. S. Kim, *J. Mater. Chem. A*, 2021, **9**, 3511–3519.
23 M. Umer, S. Umer, M. Zafari, M. Ha, R. Anand, A. Hajibabaei, A. Abbas, G. Lee and K. S. Kim, *J. Mater. Chem. A*, 2022, **10**, 6679–6689.
24 D. A. Augusto and H. J. C. Barbosa, in *Proceedings*, Sixth Brazilian Symposium on Neural Networks, 2000, vol. 1, pp. 173–178.
25 B. Weng, Z. Song, R. Zhu, Q. Yan, Q. Sun, C. G. Grice, Y. Yan and W.-J. Yin, *Nat. Commun.*, 2020, **11**, 3513.
26 P. Neumann, L. Cao, D. Russo, V. S. Vassiliadis and A. A. Lapkin, *Chem. Eng. J.*, 2020, **387**, 123412.
27 B. K. Petersen, M. L. Larma, T. N. Mundhenk, C. P. Santiago, S. K. Kim and J. T. Kim, arXiv:1912.04871[cs, stat].
28 L. J. Enman, M. B. Stevens, M. H. Dahan, M. R. Nellist, M. C. Toroker and S. W. Boettcher, *Angew. Chem., Int. Ed.*, 2018, **130**, 13022–13026.
29 M. B. Stevens, C. D. M. Trang, L. J. Enman, J. Deng and S. W. Boettcher, *J. Am. Chem. Soc.*, 2017, **139**, 11361–11364.
30 L. Trotochaud, S. L. Young, J. K. Ranney and S. W. Boettcher, *J. Am. Chem. Soc.*, 2014, **136**, 6744–6753.
31 I. Spanos, A. A. Auer, S. Neugebauer, X. Deng, H. Tüysüz and R. Schlögl, *ACS Catal.*, 2017, **7**, 3768–3778.
32 G. Dong, M. Fang, H. Wang, S. Yip, H.-Y. Cheung, F. Wang, C.-Y. Wong, S. Tak Chu and J. C. Ho, *J. Mater. Chem. A*, 2015, **3**, 13080–13086.
33 R. Chen, C. Yang, W. Cai, H.-Y. Wang, J. Miao, L. Zhang, S. Chen and B. Liu, *ACS Energy Lett.*, 2017, **2**, 1070–1075.
34 S. Anantharaj, S. R. Ede, K. Karthick, S. Sam Sankar, K. Sangeetha, P. E. Karthik and S. Kundu, *Energy Environ. Sci.*, 2018, **11**, 744–771.
35 T. Wang, X. Li, Y. Pang, X. Gao, Z. Kou, J. Tang and J. Wang, *Chem. Eng. J.*, 2021, **425**, 131491.
36 A. J. Tkalych, H. L. Zhuang and E. A. Carter, *ACS Catal.*, 2017, 11.
37 P. Gono and A. Pasquarello, *J. Chem. Phys.*, 2021, **154**, 024706.
38 H. Xiao, H. Shin and W. A. Goddard, *Proc. Natl. Acad. Sci. U. S. A.*, 2018, **115**, 5872–5877.
39 J. M. P. Martirez and E. A. Carter, *J. Am. Chem. Soc.*, 2019, **141**, 693–705.
40 S. Kang, K. Ham, H.-K. Lim and J. Lee, *Electrochim. Acta*, 2021, **386**, 138401.
41 K. Wang, H. Du, S. He, L. Liu, K. Yang, J. Sun, Y. Liu, Z. Du, L. Xie, W. Ai and W. Huang, *Adv. Mater.*, 2021, **33**, 2005587.
42 P. Yan, Q. Liu, H. Zhang, L. Qiu, H. Bin Wu and X.-Y. Yu, *J. Mater. Chem. A*, 2021, **9**, 15586–15594.
43 O. Piqué, F. Illas and F. Calle-Vallejo, *Phys. Chem. Chem. Phys.*, 2020, **22**, 6797–6803.
44 I. C. Man, H.-Y. Su, F. Calle-Vallejo, H. A. Hansen, J. I. Martínez, N. G. Inoglu, J. Kitchin, T. F. Jaramillo, J. K. Nørskov and J. Rossmeisl, *ChemCatChem*, 2011, **3**, 1159–1165.
45 M. Retuerto, L. Pascual, F. Calle-Vallejo, P. Ferrer, D. Gianolio, A. G. Pereira, Á. García, J. Torrero, M. T. Fernández-Díaz, P. Bencok, M. A. Peña, J. L. G. Fierro and S. Rojas, *Nat. Commun.*, 2019, **10**, 2041.
46 M. García-Mota, A. Vojvodic, H. Metiu, I. C. Man, H.-Y. Su, J. Rossmeisl and J. K. Nørskov, *ChemCatChem*, 2011, **3**, 1607–1611.
47 M. Retuerto, F. Calle-Vallejo, L. Pascual, G. Lumbeeck, M. T. Fernandez-Diaz, M. Croft, J. Gopalakrishnan, M. A. Peña, J. Hadermann, M. Greenblatt and S. Rojas, *ACS Appl. Mater. Interfaces*, 2019, **11**, 21454–21464.
48 F. Calle-Vallejo, J. Ignacio Martínez and J. Rossmeisl, *Phys. Chem. Chem. Phys.*, 2011, **13**, 15639–15643.
49 S. Lee, L. Bai and X. Hu, *Angew. Chem., Int. Ed.*, 2020, **132**, 8149–8154.